Editors' Suggestion

# Probing a Defect-Site-Specific Electronic Orbital in Graphene with Single-Atom Sensitivity

Mingquan Xu,[1] Aowen Li,[1] Stephen J. Pennycook,[1] Shang-Peng Gao,[2,*] and Wu Zhou[1,†]
[1]School of Physical Sciences and CAS Key Laboratory of Vacuum Physics, University of Chinese Academy of Sciences, Beijing 100049, People's Republic of China
[2]Department of Materials Science, Fudan University, Shanghai, 200433, People's Republic of China

(Received 7 April 2023; accepted 5 September 2023; published 31 October 2023)

Visualization of individual electronic states ascribed to specific unoccupied orbitals at the atomic scale can reveal fundamental information about chemical bonding, but it is challenging since bonding often results in only subtle variations in the whole density of states. Here, we utilize atomic-resolution energy-loss near-edge fine structure (ELNES) spectroscopy to map out the electronic states attributed to specific unoccupied $p_z$ orbital around a fourfold coordinated silicon point defect in graphene, which is further supported by theoretical calculations. Our results illustrate the power of atomic-resolution ELNES towards the probing of defect-site-specific electronic orbitals in monolayer crystals, providing insights into understanding the effect of chemical bonding on the local properties of defects in solids.

DOI: 10.1103/PhysRevLett.131.186202

Electronic orbitals reflect the chemical bonding of matter, thus primarily determining the physical and chemical properties of materials. Real-space observation of electronic orbitals at the atomic scale can correlate the bonding information with the local atomic configuration directly, which is of fundamental importance for understanding macroscopic properties and exploring novel functionalities in new materials. Some reconstruction methods through photoemission spectroscopy [1] and x-ray or electron diffraction [2,3] have been developed to obtain information about orbitals, but they generally suffer from the lack of atomic resolution. Besides, scanning tunneling microscopy (STM) [4,5] and noncontact atomic force microscopy (nc-AFM) [6] can implement the direct observation of individual electronic states and chemical bonds, which, however, are limited to absorbed molecules on specific substrates or delaminated surfaces. Therefore, exploration of new versatile approaches to the atomic-scale observation of electronic orbitals in real space is still urgently needed.

With the advent of aberration correctors in (scanning) transmission electron microscopy [(S)TEM], atomic-resolution detection of bonding has become routinely available. Reconstruction of high-resolution TEM images [7] and advanced four-dimensional STEM [8,9] can map out the charge density distribution, which contains information of chemical bonding, at the atomic scale, but lacks the ability for elemental identification. Energy-loss near-edge fine structure (ELNES) in electron energy-loss spectroscopy (EELS) can reveal the energy-dependent transitions from initial core states to specific unoccupied orbitals or states in the given excited atoms, adding the element-specific information in STEM with atomic resolution [10–12]. It was theoretically predicted that atomic-resolved mapping of electronic orbitals can be achieved by EELS in aberration-corrected STEM [13], and subsequently, some experimental results have been reported with bulk specimens [14–16]. Nevertheless, neighboring atomic columns inevitably disturb the direct interpretation of electronic orbital mapping in bulk materials due to the channeling effect of inelastic scattering [17,18]. Therefore, monolayer crystals are considered to be a good platform for accurate probing of the electronic orbitals [19] at the atomic scale, but the weak scattering of incident electrons from monolayer samples is the main suffering for high-quality ELNES measurement. Significant effort has been devoted to explore the impact of local bonding on monolayer graphene using ELNES [20–22], but thus far, the real-space probing of electronic orbitals with single-atom sensitivity still remains extremely challenging.

In this Letter, we successfully visualized individual unoccupied electronic states, which are ascribed to the unoccupied carbon $p_z$ orbitals in monolayer defective graphene by using atomic-resolution ELNES spectroscopy in a low-voltage aberration-corrected STEM. With the optimized EELS acquisition of a direct electron detector, high-quality ELNES mapping with a good signal-to-noise ratio per pixel has been achieved. This approach enables the atom-by-atom analysis of a specific signal in the ELNES of the carbon-$K$ edge around a substitutional silicon atom with fourfold coordination in graphene. Complementary with theoretical calculations, this specific signal is determined to originate from a $p_z$-like orbital perpendicular to the graphene basal plane. The direct mapping-out of unoccupied electronic states attributed to the defect-specific electronic orbitals with single-atom sensitivity provides new possibilities to explore defect physics in graphene.

 

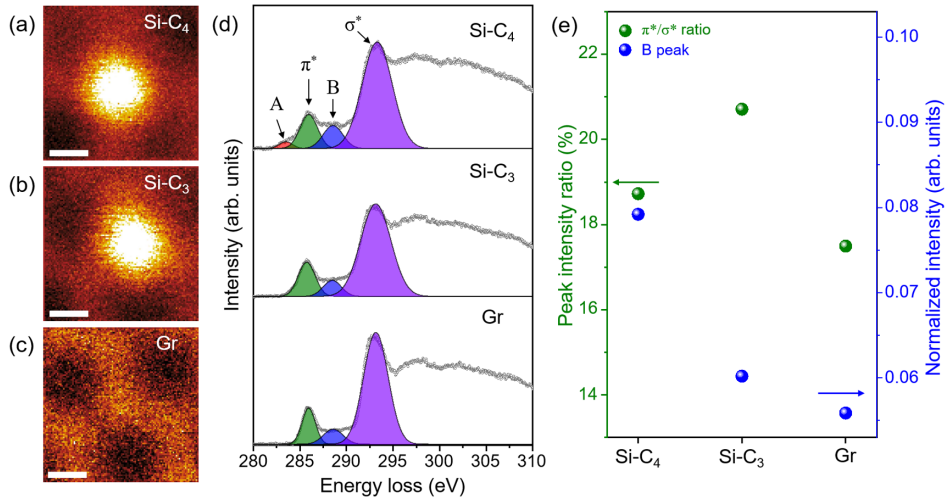


FIG. 1. ELNES analysis of Si—$C_4$, Si—$C_3$ and graphene. The simultaneously acquired ADF-STEM images of the Si—$C_4$ (a), Si—$C_3$ (b) and Gr (c) during the EELS acquisition. (d) The accumulated EEL spectra of Si—$C_4$, Si—$C_3$ and Gr. The pre-peak before the $\pi^*$ peak in Si—$C_4$ is labeled as $A$ and the bump between $\pi^*$ and $\sigma^*$ peaks is labeled as $B$. (e) The intensity ratios of $\pi^*$ to $\sigma^*$ peak and the normalized intensities of the $B$ peak in the three different configurations. The normalized intensities mean normalization to the integrated intensity in the continuum of $300-310$ eV. Scale bars: 0.1 nm.

In order to obtain high-quantity ELNES spectra at the atomic scale for reliable interpretation, the geometric aberrations and monochromator aberrations in our Nion HERMES microscope were carefully tuned to achieve atomic resolution at 60 kV with a high probe current of 100 pA (in Supplemental Material, Fig. S1 [23]). This ensures a good signal-to-noise ratio in the atomic-scale ELNES experiment on monolayer samples. In Figs. 1(a)–1(d), we used a subscan window ($0.4 \times 0.4$ nm$^2$) to cover the silicon (Si) impurity atoms and their nearest-neighboring carbon atoms in fourfold coordinated and threefold coordinated Si point defects (denoted as Si—$C_4$ and Si—$C_3$, respectively), and acquired accumulated ELNES spectra at the atomic scale on the two types of the Si point defect (see Supplemental Material for details [23]). The ELNES spectrum of the pristine graphene (Gr) as the reference in Fig. 1(d) was collected by the same method.

After background subtraction, the ELNES spectra of the three different structures are illustrated in Fig. 1(d) with two dominant peaks (labeled as $\pi^*$ and $\sigma^*$) at approximately 286.0 and 293.2 eV (in Supplemental Material, Table S1 [23]), reflecting the transitions of inner shell electrons from $1s$ states to the empty $\pi^*$ and $\sigma^*$ antibonding states of carbon atoms in graphene, respectively. Line shape analysis [33,34] was applied to explore the underlying information in ELNES. In Fig. 1(e), the intensity ratios between $\pi^*$ and $\sigma^*$ peaks in the Si—$C_4$ and Si—$C_3$ defects are higher than that in pristine graphene, indicating that the substitution of the Si impurity atoms breaks the perfect $sp^2$ hybridization in the graphene lattice, especially in the buckled Si—$C_3$ defect. Furthermore, the bump between the $\pi^*$ and $\sigma^*$ peaks [labeled as $B$ in Fig. 1(d)] shows most strongly in the Si—$C_4$ configuration. As this peak is often indicative of the C—$M$ bonding ($M$ represents other elements) in carbon compounds [35,36], we presume that the maximized $B$ peak in Si—$C_4$ reflects the specific Si—C bonding correspondingly. Besides, it is noteworthy that, in the Si—$C_4$ defect configuration, a distinct pre-peak [labeled as $A$ in Fig. 1(d)] emerges at 283.5 eV before the $\pi^*$ peak, which is absent in the other two structures. The above analysis demonstrates that our ELNES measurement is able to detect subtle variations in local density of states around individual atoms due to the specific local bonding configuration in graphene.

To elucidate the correlation between the unique spectroscopic signatures and the local bonding configuration in the Si—$C_4$ defect, atomically resolved ELNES mapping was further performed. The direct electron EELS detector (DECTRIS ELA) [25], which is free of readout noise, was employed to collect the multiple spectrum images with low exposure time per pixel, enabling significant improvement in the signal-to-noise ratio of atomic-scale ELNES mapping and also minimizing the deleterious effects of electron beam irradiation (see details in Methods). The simultaneously acquired annular dark-field (ADF) sequential images during the EELS mapping (in Supplemental Material, Fig. S2 [23]) demonstrate that the structure of the Si—$C_4$ defect remained damage-free within the EELS acquisition. Figure 2(a) is the atomic-resolution ADF image integrated from the sequential images in Supplemental Material, Fig. S2 [23], which can provide the precise atomic positions for the atom-by-atom ELNES analysis. The neighboring carbon atoms around the Si impurity in Si—$C_4$ are categorized into three groups based on their distances from the Si impurity: the first-neighboring carbon (1st C, labeled in red), the second-neighboring carbon in pentagons (2nd C, labeled in green) and the

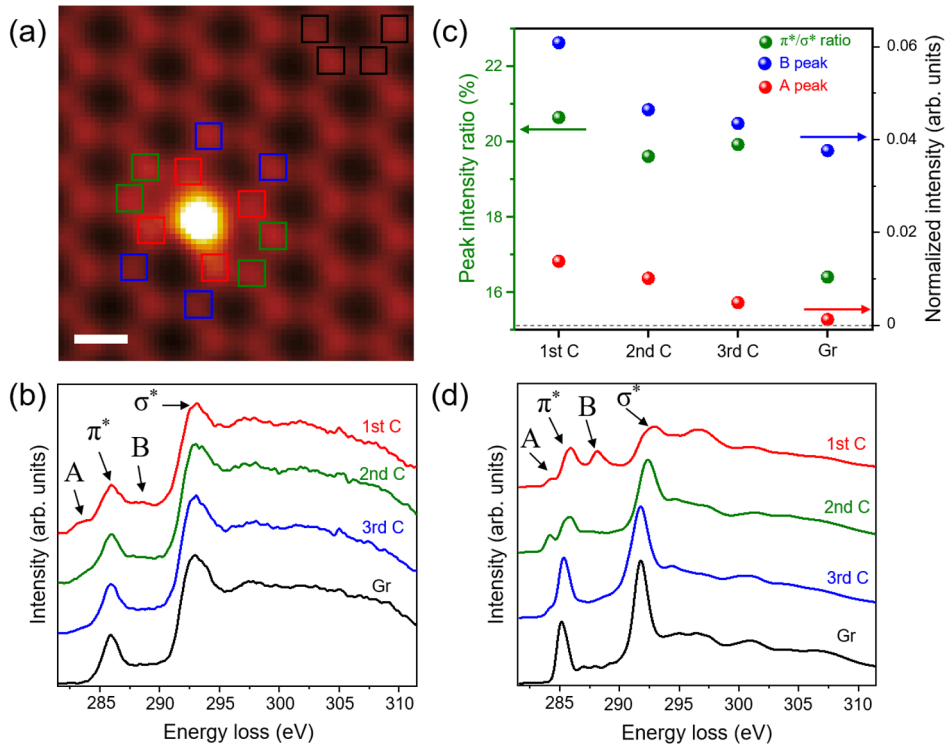


FIG. 2. Atom-by-atom ELNES analysis of Si—$C_4$. (a) The simultaneously acquired ADF-STEM image during the EELS mapping, as a reference image for the atom-by-atom analysis. The first-neighboring carbon atoms (1st C) are labeled in red. The second-neighboring carbon in pentagons atoms (2nd C) are labeled in green. The second-neighboring carbon in distorted hexagons atoms (3rd C) are labeled in blue. The carbon atoms far away from the Si atom are chosen to represent pristine graphene (Gr), which are labeled in black. (b) The ELNES spectra of different carbon atoms in Si—$C_4$. (c) The intensity ratios between $\pi^*$ and $\sigma^*$ peaks of different carbon atoms in Si—$C_4$. The normalized intensities of $A$ and $B$ peaks of different carbon atoms in Si—$C_4$, normalized to the integrated intensity in the continuum of 300–310 eV. (d) The calculated ELNES spectra of different carbon atoms in Si—$C_4$. The calculated ELNES spectrum of pristine graphene is used as a reference. All calculated spectra are rigidly translated without stretching of the energy axis. Scale bar: 0.2 nm.

second-neighboring carbon in distorted hexagons (3rd C, labeled in blue). In addition, the EEL spectra extracted from four carbon atoms (Gr, labeled in black) far away from the Si impurity in Si—$C_4$ are chosen as the reference spectrum of pristine graphene.

The atom-by-atom extracted ELNES spectra in Fig. 2(b) and the corresponding line shape analysis in Fig. 2(c) demonstrate the evolution of the ELNES signatures across the Si—$C_4$ point defect. In agreement with the results in Fig. 1, the substitutional Si impurity in the Si—$C_4$ defect disrupts the perfect $sp^2$ hybridization in the graphene lattice, reflected in higher $\pi^*/\sigma^*$ ratios for the carbon atoms around the Si—$C_4$ defect (from the 1st C to the 3rd C) than that in pristine graphene (Gr), as shown in Fig. 2(c). In addition, the $B$ peak, which is located between the $\pi^*$ and $\sigma^*$ peaks, shows a significantly higher intensity on the 1st C atom but a dramatic decrease on the 2nd and 3rd carbons, reflecting the high localization of the corresponding excited state. The intensities of the distinct $A$ peak exhibit a gradual damping from the 1st C to the 3rd C, and finally become absent in the pristine graphene [Gr in Fig. 2(b)], reflecting that the corresponding excited state is considerably delocalized in real space. Therefore, the single-atom ELNES spectroscopy of the Si—$C_4$ defect with atom-by-atom analysis demonstrates that the isovalent substitution of Si impurity with the fourfold coordination exerts a significant impact on the local bonding environments of carbon atoms around the silicon.

Several previous works have shown that the presence of dangling bonds on carbon atoms can lead to additional signals before the $\pi^*$ peak in C-$K$ EELS edge [20], which, however, is insufficient to account for our observation of the distinct $A$ peak since there are no dangling bonds in the Si—$C_4$ configuration. To provide a theoretical interpretation for the new features in our experimental ELNES spectra, the simulation of ELNES spectra of the Si—$C_4$ configuration and pristine graphene, based on density functional theory (DFT) calculations, was conducted and shown in Fig. 2(d). The main features in experimental ELNES are successfully reproduced in the calculated counterparts. Specifically, the calculated ELNES spectra from the 1st C to 3rd C in Si—$C_4$ show considerable intensities in the energy-loss range related to the $A$ peak, compared with that of pristine graphene. In addition, the intensity of the

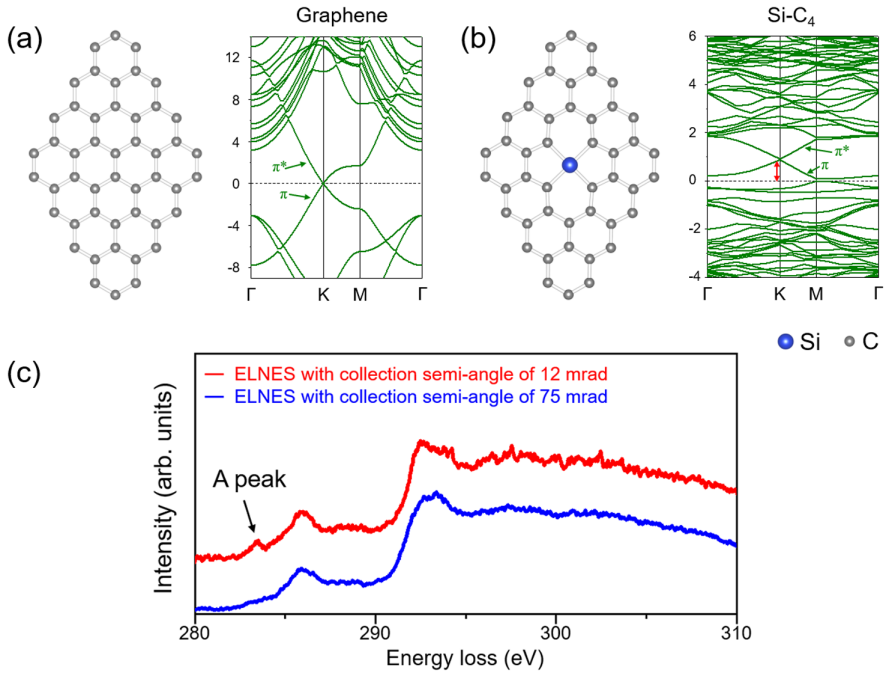


FIG. 3. Theoretical explanation for the origin of the $A$ peak. (a) The atomic schematic and calculated band structure of graphene. (b) The atomic schematic and calculated band structure of Si—$C_4$. The Fermi level is indicated at 0 eV by the dashed lines and the red arrow in (b) highlights the gap between the Fermi level and the Dirac node at the $K$ point. (c) Experimental ELNES spectra of Si—$C_4$ with different EELS collection semiangles by the acquisition method as the same as that in Fig. 1. Spectra are aligned with the center of the $\pi^*$ peak.

calculated $B$ peak is highly localized on the 1st C, which is consistent with the experimental results.

To further reveal the physics behind the ELNES features, the band structures of the pristine graphene and Si—$C_4$ supercell were calculated, as shown in Figs. 3(a) and 3(b). The Fermi level of pristine graphene [in Fig. 3(a)] intersects with the Dirac nodes at the $K$ point, giving rise to the semimetallic nature of graphene [37]. However, compared with pristine graphene, the substitutional Si atom bonded with four carbon atoms at a double-vacancy site in the Si—$C_4$ configuration generates a deficiency of four valence electrons, thus resulting in a downshift of the Fermi level relative to the Dirac nodes at the $K$ point [highlighted by the red arrow in Fig. 3(b)]. This leaves the $\pi$ bonding states between the Dirac nodes and Fermi level unoccupied, which accounts for the origin of the distinct $A$ peak observed in the ELNES spectra of Si—$C_4$ [38,39]. The calculation of local density of states on the 1st carbon in Si—$C_4$ further confirms the origin of the observed $A$ peak in the Si—$C_4$ defect, as shown in Supplemental Material, Fig. S3(b) [23]. Moreover, the $\pi$ bonding state in graphene reflects the $p_z$ orbital perpendicular to the basal plane of graphene. The orientation dependence of core-loss EELS spectra of anisotropic materials can be described using contributions with momentum transfer parallel ($\epsilon^{\parallel}$) and perpendicular ($\epsilon^{\perp}$) to the electron beam generally as [40]:

$$I(\Delta E) = a\epsilon^{\parallel} + b\epsilon^{\perp},$$

where $\Delta E$ is the energy loss, and $a$ and $b$ are the corresponding weighting factors. When the crystallographic $c$ axis of graphene is parallel to the electron beam, the polarized components of DFT-calculated ELNES spectrum on the 1st C atoms (as shown in Supplemental Material, Fig. S3 [23]) demonstrates that the $A$ peak, which corresponds to the electronic transitions to the unoccupied $p_z$ orbitals, features momentum transfer parallel to the electron beam and should contribute more to the total EEL spectrum with the decreased EELS collection angle [41]. Therefore, under our experimental conditions where the incident electron beam is roughly parallel to the crystallographic $c$ axis of graphene, an increased relative contribution of the parallel component should be observed with a smaller EELS collection aperture. Specifically, a more prominent appearance of $A$ peak is observed under the smaller collection semiangle of 12 mrad compared to that of 75 mrad, as illustrated in Fig. 3(c).

Furthermore, in order to demonstrate the spatial extension of specific unoccupied electronic states around the Si—$C_4$ defect, atomic-resolution ELNES mapping was performed, as shown in Fig. 4. Figure 4(a) is the simultaneously-acquired ADF image during the EELS mapping,

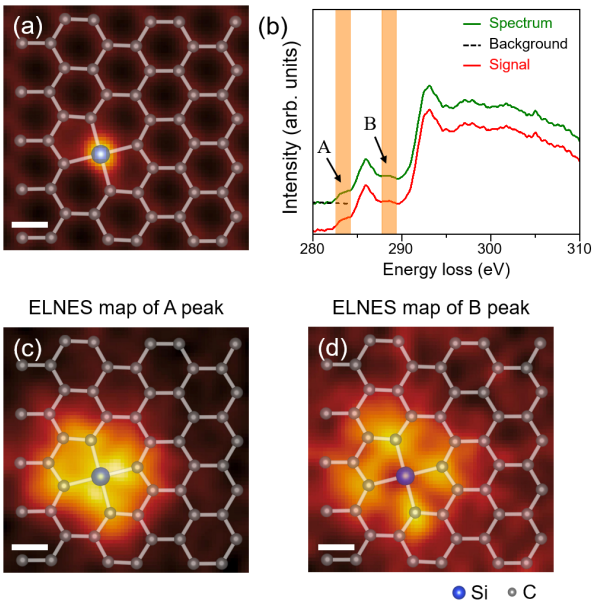


FIG. 4. ELNES maps of the $A$ and $B$ peaks in the Si—$C_4$ configuration. (a) Representation of the simultaneously acquired STEM-ADF during EELS mapping shown in Fig. 2, overlaid with the Si—$C_4$ atomic model. (b) A typical ELNES spectrum extracted from the 1st C atoms of the Si—$C_4$ defect configuration. Two orange regions label the energy windows of $A$ and $B$ peaks for the maps in (c) and (d), respectively. (c) The ELNES map of the $A$ peak, overlaid with the Si—$C_4$ atomic model. (d) The ELNES map of the $B$ peak, overlaid with the Si—$C_4$ atomic model. Scale bars: 0.2 nm.

and Fig. 4(b) demonstrates the two energy windows for the ELNES maps in Figs. 4(c) and 4(d). The map of the $A$ peak in Fig. 4(c) displays a dispersed contrast across the Si—$C_4$ point defect, and the map of the $B$ peak in Fig. 4(d) shows a highly localized enhancement in contrast on the 1st carbon atoms. The probe size in our ELNES experiment and the EELS delocalization of the carbon $K$ edge are approximately 1.2 and 2.3 Å, respectively, which are comparable to the Si—C bond length of ~1.9 Å in the Si—$C_4$ structure. Consequently, the effects of probe tail and signal delocalization, as well as the spatial extension of the final unoccupied states, together influence the spatial distribution of signals in the ELNES mapping in Figs. 4(c) and 4(d), i.e., the probe on the Si atom could also excite the surrounding four 1st C atoms. In addition, comparison of the ELNES maps of $A$ peak and $B$ peak suggests that the carbon $p_z$ orbitals contributing to the final states of the $A$ peak have a high degree of hybridization with the Si orbitals at the Si defect site. Therefore, the atomic-scale ELNES mapping with reliable signal-to-noise ratio per pixel in our study illustrates its capability towards the visualization of electronic states attributed to specific unoccupied orbitals with the single-atom sensitivity.

In summary, we have successfully visualized individual electronic states at the Si—$C_4$ point defect in graphene via two-dimensional ELNES spectroscopic imaging at atomic resolution. Our combined experimental results and theoretical calculations verified that the distinct pre-peak in carbon-$K$ edge originates from the unoccupied $\pi$ bonding states between the Dirac nodes and Fermi level, which is caused by the downshift of the Fermi level in the electron-deficient Si—$C_4$ configuration. Our study highlights the potential of real-space mapping of specific electronic excitations at the single-atom scale through the high-quality ELNES imaging, e.g., visualizing spin states or magnetic moments in real space, and could lead to new insights into the functionalization of quantum devices through defect engineering.

This research was supported by the National Key R&D Program of China (2018YFA0305800), the Beijing Outstanding Young Scientist Program (BJJWZYJH01201914430039), and the CAS Project for Young Scientists in Basic Research (YSBR-003). We thank Ms. Dongqian Meng for preparing the graphene sample and Professor Wei Ji for discussion. W. Z. supervised this project. M. X. carried out the STEM-EELS experiments and the analysis of ELNES data with the help from A. L. The first-principle DFT calculations were performed by S. G. M. X. wrote the paper with the input from A. L. and S. J. P. All authors discussed the results and commented on the manuscript.

*Corresponding author: gaosp@fudan.edu.cn
†Corresponding author: wuzhou@ucas.ac.cn

[1] P. Puschnig, S. Berkebile, A. J. Fleming, G. Koller, K. Emtsev, T. Seyller, J. D. Riley, C. Ambrosch-Draxl, F. P. Netzer, and M. G. Ramsey, Science **326**, 702 (2009).
[2] T. S. Koritsanszky and P. Coppens, Chem. Rev. **101**, 1583 (2001).
[3] J. M. Zuo, M. Kim, M. O'Keeffe, and J. C. H. Spence, Nature (London) **401**, 49 (1999).
[4] J. Repp, G. Meyer, S. M. Stojković, A. Gourdon, and C. Joachim, Phys. Rev. Lett. **94**, 026803 (2005).
[5] L. Gross, N. Moll, F. Mohn, A. Curioni, G. Meyer, F. Hanke, and M. Persson, Phys. Rev. Lett. **107**, 086101 (2011).
[6] P. Chen, D. Fan, A. Selloni, E. A. Carter, C. B. Arnold, Y. Zhang, A. S. Gross, J. R. Chelikowsky, and N. Yao, Nat. Commun. **14**, 1460 (2023).
[7] J. C. Meyer *et al.*, Nat. Mater. **10**, 209 (2011).
[8] N. Shibata, T. Seki, G. Sánchez-Santolino, S. D. Findlay, Y. Kohno, T. Matsumoto, R. Ishikawa, and Y. Ikuhara, Nat. Commun. **8**, 15631 (2017).
[9] W. Gao *et al.*, Nature (London) **575**, 480 (2019).
[10] R. F. Egerton, Rep. Prog. Phys. **72**, 016502 (2008).
[11] K. Suenaga, M. Tencé, C. Mory, C. Colliex, H. Kato, T. Okazaki, H. Shinohara, K. Hirahara, S. Bandow, and S. Iijima, Science **290**, 2280 (2000).
[12] H. Tan, S. Turner, E. Yücelen, J. Verbeeck, and G. Van Tendeloo, Phys. Rev. Lett. **107**, 107602 (2011).

[13] S. Löffler, V. Motsch, and P. Schattschneider, Ultramicroscopy **131**, 39 (2013).
[14] S. Löffler, M. Bugnet, N. Gauquelin, S. Lazar, E. Assmann, K. Held, G. A. Botton, and P. Schattschneider, Ultramicroscopy **177**, 26 (2017).
[15] C. Iwashimizu, M. Haruta, and H. Kurata, Appl. Phys. Lett. **119**, 232902 (2021).
[16] M. Bugnet, M. Ederer, V. K. Lazarov, L. Li, Q. M. Ramasse, S. Löffler, and D. M. Kepaptsoglou, Phys. Rev. Lett. **128**, 116401 (2022).
[17] K. Kimoto, K. Ishizuka, and Y. Matsui, Micron **39**, 257 (2008).
[18] M. J. Neish, N. R. Lugg, S. D. Findlay, M. Haruta, K. Kimoto, and L. J. Allen, Phys. Rev. B **88**, 115120 (2013).
[19] L. Pardini, S. Löffler, G. Biddau, R. Hambach, U. Kaiser, C. Draxl, and P. Schattschneider, Phys. Rev. Lett. **117**, 036801 (2016).
[20] K. Suenaga and M. Koshino, Nature (London) **468**, 1088 (2010).
[21] W. Zhou, M. D. Kapetanakis, M. P. Prange, S. T. Pantelides, S. J. Pennycook, and J.-C. Idrobo, Phys. Rev. Lett. **109**, 206803 (2012).
[22] Q. M. Ramasse, C. R. Seabourne, D.-M. Kepaptsoglou, R. Zan, U. Bangert, and A. J. Scott, Nano Lett. **13**, 4989 (2013).
[23] See Supplemental Material at http://link.aps.org/supplemental/10.1103/PhysRevLett.131.186202 for detailed methods and additional information. The Supplemental Material also contains Refs. [24–32].
[24] X. Li *et al.*, Science **324**, 1312 (2009).
[25] B. Plotkin-Swing *et al.*, Ultramicroscopy **217**, 113067 (2020).
[26] C. Meyer, N. Dellby, J. A. Hachtel, T. Lovejoy, A. Mittelberger, and O. Krivanek, Microsc. Microanal. **25**, 122 (2019).
[27] F. d. l. Peña *et al.*, Hyperspy/Hyperspy: HyperSpy v1.5.2. (2022), hyperspy/hyperspy: Release v1.7.3 (Version v1.7.3), 10.5281/zenodo.7263263.
[28] G. Kresse and J. Furthmüller, Comput. Mater. Sci. **6**, 15 (1996).
[29] G. Kresse and J. Furthmüller, Phys. Rev. B **54**, 11169 (1996).
[30] J. Sun *et al.*, Nat. Chem. **8**, 831 (2016).
[31] S.-P. Gao, C. J. Pickard, M. C. Payne, J. Zhu, and J. Yuan, Phys. Rev. B **77**, 115122 (2008).
[32] S.-P. Gao, C. J. Pickard, A. Perlov, and V. Milman, J. Phys. Condens. Matter **21**, 104203 (2009).
[33] R. Senga, T. Pichler, and K. Suenaga, Nano Lett. **16**, 3661 (2016).
[34] A. J. Papworth, C. J. Kiely, A. P. Burden, S. R. P. Silva, and G. A. J. Amaratunga, Phys. Rev. B **62**, 12628 (2000).
[35] A. Tararan, A. Zobelli, A. M. Benito, W. K. Maser, and O. Stéphan, Chem. Mater. **28**, 3741 (2016).
[36] S. G. Minasian, J. M. Keith, E. R. Batista, K. S. Boland, S. A. Kozimor, R. L. Martin, D. K. Shuh, T. Tyliszczak, and L. J. Vernon, J. Am. Chem. Soc. **135**, 14731 (2013).
[37] A. K. Geim and K. S. Novoselov, Nat. Mater. **6**, 183 (2007).
[38] N. Nilforoushan *et al.*, Proc. Natl. Acad. Sci. U.S.A. **118**, e2108617118 (2021).
[39] D. Kepaptsoglou *et al.*, ACS Nano **9**, 11398 (2015).
[40] N. D. Browning, J. Yuan, and L. M. Brown, Ultramicroscopy **38**, 291 (1991).
[41] R. F. Klie, H. Su, Y. Zhu, J. W. Davenport, J.-C. Idrobo, N. D. Browning, and P. D. Nellist, Phys. Rev. B **67**, 144508 (2003).